AGU PUBLICATIONS

JGR

Journal of Geophysical Research: Solid Earth

RESEARCH ARTICLE
10.1002/2015JB012516

Key Points:
- We use coseismic, postseismic, and interseismic data from the Imperial Fault to model its frictional properties
- Geodetic data suggest a significant strain rate asymmetry across the Imperial Fault
- We propose a second active fault connecting the San Jacinto and Cerro Prieto faults to the west

Correspondence to:
E. O. Lindsey,
elindsey@ntu.edu.sg

Citation:
Lindsey, E. O., and Y. Fialko (2016), Geodetic constraints on frictional properties and earthquake hazard in the Imperial Valley, southern California, *J. Geophys. Res. Solid Earth*, *121*, 1097–1113, doi:10.1002/2015JB012516.

Received 9 SEP 2015
Accepted 18 JAN 2016
Accepted article online 25 JAN 2016
Published online 5 FEB 2016

Geodetic constraints on frictional properties and earthquake hazard in the Imperial Valley, Southern California

Eric O. Lindsey[1,2] and Yuri Fialko[1]

[1] Institute of Geophysics and Planetary Physics, Scripps Institution of Oceanography, University of California San Diego, La Jolla, California, USA, [2] Earth Observatory of Singapore, Nanyang Technological University, Singapore

Abstract We analyze a suite of geodetic observations across the Imperial Fault in southern California that span all parts of the earthquake cycle. Coseismic and postseismic surface slips due to the 1979 *M* 6.6 Imperial Valley earthquake were recorded with trilateration and alignment surveys by Harsh (1982) and Crook et al. (1982), and interseismic deformation is measured using a combination of multiple interferometric synthetic aperture radar (InSAR)-viewing geometries and continuous and survey-mode GPS. In particular, we combine more than 100 survey-mode GPS velocities with InSAR data from Envisat descending tracks 84 and 356 and ascending tracks 77 and 306 (149 total acquisitions), processed using a persistent scatterers method. The result is a dense map of interseismic velocities across the Imperial Fault and surrounding areas that allows us to evaluate the rate of interseismic loading and along-strike variations in surface creep. We compare available geodetic data to models of the earthquake cycle with rate- and state-dependent friction and find that a complete record of the earthquake cycle is required to constrain key fault properties including the rate-dependence parameter ($a - b$) as a function of depth, the extent of shallow creep, and the recurrence interval of large events. We find that the data are inconsistent with a high (>30 mm/yr) slip rate on the Imperial Fault and investigate the possibility that an extension of the San Jacinto-Superstition Hills Fault system through the town of El Centro may accommodate a significant portion of the slip previously attributed to the Imperial Fault. Models including this additional fault are in better agreement with the available observations, suggesting that the long-term slip rate of the Imperial Fault is lower than previously suggested and that there may be a significant unmapped hazard in the western Imperial Valley.

1. Introduction

Over the past several decades, laboratory and theoretical studies have led to the development of constitutive relations governing fault friction [*Dieterich*, 1978; *Ruina*, 1983; *Rice and Ruina*, 1983; *Marone et al.*, 1991]. These relations, known as rate- and state-dependent friction theory, accurately reproduce many observed features of active faults such as spontaneous earthquake nucleation, stick-slip behavior, and shallow creep [*Tse and Rice*, 1986; *Marone and Scholz*, 1988; *Scholz*, 1998; *Lapusta et al.*, 2000; *Lapusta and Rice*, 2003] and with some modifications, episodic slow slip events [*Liu and Rice*, 2007; *Colella et al.*, 2011; *Hawthorne and Rubin*, 2013; *Wei et al.*, 2013].

Numerical models incorporating the rate-state (RS) formalism produce repeating periodic or quasiperiodic sequences of events with many features matching those observed in nature [e.g., *Barbot et al.*, 2012]. The RS earthquake cycle models depend on laboratory-derived values of key frictional parameters, which are determined at conditions that do not always correspond to those in natural settings [*Baumberger and Caroli*, 2006; *Scholz*, 2007]. In a recent study, *Kaneko et al.* [2013] attempted to infer in situ parameters by fitting earthquake cycle models to geodetic data across the partially creeping Izmit segment of the North Anatolian Fault. *Kaneko et al.* [2013] found that commonly assumed values of the friction parameters can provide a reasonable fit to the late interseismic data, but the models are highly nonunique due to poor constraints on the temporal evolution of the rate of surface creep during the early part of the earthquake cycle. In this study we apply the RS earthquake cycle model to a set of geodetic observations from the Imperial Fault in Southern California and northern Baja California, Mexico that span all parts of the earthquake cycle.

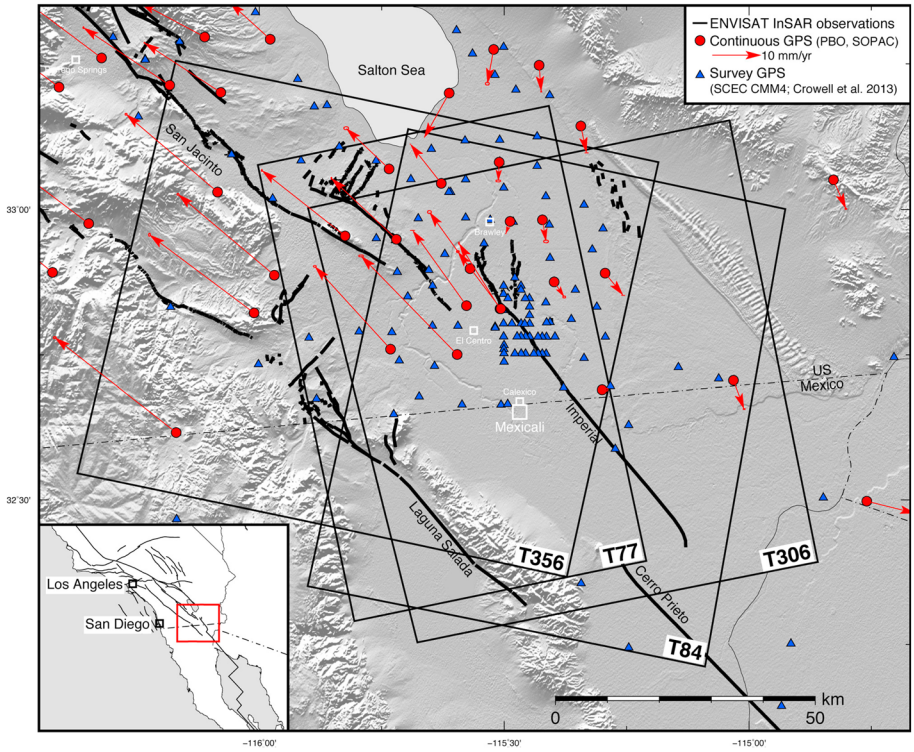

Figure 1. Map showing the study area and nearby faults. Thick black lines with labels denote active faults mapped by the USGS (http://earthquake.usgs.gov/hazards/qfaults/). Rectangular outlines show the extent of the Envisat InSAR data used in this study. Red dots with vectors show continuous GPS stations with velocity solutions from the Plate Boundary Observatory (PBO, http://pbo.unavco.org/data/gps) and the Scripps Orbit and Permanent Array Center (SOPAC, http://sopac.ucsd.edu). Blue triangles denote locations of survey-mode GPS monuments from *Shen et al.* [2011] and *Crowell et al.* [2013]. Inset map shows the location in Southern California. Figures were prepared using the Generic Mapping Tools (GMT) software [*Wessel et al.*, 2013].

The Imperial Fault has hosted several large earthquakes in the past century, the most recent of which was well observed geodetically. The 15 October 1979 M_w 6.5 Imperial Valley earthquake ruptured the northern 30 km of the fault, from just north of the U.S.-Mexico border past the intersection with the Brawley Fault, and also triggered some slip on the Brawley Fault (Figure 1). Along with detailed mapping of the coseismic surface rupture, postseismic slip observations were collected at several locations along the fault [*Crook et al.*, 1982; *Harsh*, 1982].

A much larger (M_w 7.0) earthquake on the Imperial Fault occurred in 1940. The 1940 event ruptured the entire fault and produced up to 6 m of right-lateral slip near the international border [*Rockwell and Klinger*, 2013]. Paleoseismic evidence at the southern end of the Imperial Fault suggests relatively large recurrence intervals and surface offsets [*Thomas and Rockwell*, 1996], while evidence farther north indicates more frequent ruptures with less surface slip [*Rockwell et al.*, 2011; *Tsang et al.*, 2011].

The Imperial Fault is associated with robust shallow creep, first observed there almost 60 years ago [*Whitten*, 1956], although observations have been mostly limited to the fault section north of the border [e.g., *Lyons et al.*, 2002; *Crowell et al.*, 2013]. The creep may be steady or intermittent; one early observation associated surface displacements with a low-magnitude, low-stress-drop event [*Brune and Allen*, 1967]. In this study, we present observations which indicate that shallow creep does not extend south of the border and appears to be anticorrelated with coseismic slip from the 1940 event. We use geodetic observations of shallow fault slip that span all parts of the earthquake cycle to constrain the frictional properties of the fault. We also analyze the broader pattern of deformation and identify an active fault strand in the western Imperial Valley, first proposed by *Hogan et al.* [2002] and *Magistrale* [2002], which may account for 10–15 mm/yr of relative motion between the Pacific and North American plates.

2. Geodetic Observations

2.1. InSAR Data

We use interferometric synthetic aperture radar (InSAR) observations from the European Space Agency's Environmental Satellite (Envisat) spanning the period 2003–2010. The satellite collected a total of 149 acquisitions over four tracks covering the Imperial Fault, shown as outlines in Figure 1. There are two descending tracks (356 and 84) and two ascending tracks (77 and 306) providing a dense set of observations from several viewing geometries.

Agricultural activities and the presence of vegetation due to farming in the Imperial Valley severely affect correlation of images at the C band wavelength of 5.6 cm [e.g., *Eneva et al.*, 2013; *Wei and Sandwell*, 2010]. We therefore processed these data using a persistent scatterers method [*Hooper et al.*, 2004]. This method determines a set of stable reflectors based on their amplitude variability, given the observation that those pixels with the least variation in amplitude will also have the most stable phase properties [*Ferretti et al.*, 2001]. Interferograms for all dates relative to a single master were first calculated using the DORIS software [*Kampes et al.*, 2003], then the stable reflectors were identified and processed individually. We have identified 5×10^5 to 10^6 stable pixels for each track, for which velocities were calculated using the Small Baseline Subset (SBAS) method [*Berardino et al.*, 2002; *Schmidt and Bürgmann*, 2003].

The SBAS results contain residual long-wavelength orbital and atmospheric artifacts. We use the sum-remove-filter-restore (SURF) approach [*Tong et al.*, 2013] to remove them. Horizontal GPS velocities with uncertainties less than 0.5 mm/yr from UNAVCO Plate Boundary Observatory (PBO) and the Southern California Earthquake Center's Crustal Motion Model 4 [*Shen et al.*, 2011] were interpolated using a bicubic spline and subtracted from the average line-of-sight (LOS) velocities for each track. The results were high-pass filtered with a two-dimensional Gaussian filter at a 40 km cutoff wavelength, and then added back to the long-wavelength interpolated GPS map. Because of the filtering step, the result is minimally dependent on the interpolation method and distribution of stations, although we note that it may be less accurate south of the U.S.-Mexico border where the distribution of stations is more sparse. In this case, long-wavelength signals may be less accurately represented; however, this does not affect our primary goal of an accurate measurement of fault creep.

The estimated line-of-sight (LOS) velocities for each of the four tracks are shown in Figure 2. Using the method described by *Lindsey et al.* [2014], we may decompose the ascending and descending LOS velocities into vertical and horizontal components, provided that the horizontal direction of motion is known and relatively uniform (i.e., predominantly fault parallel). The GPS velocities shown in Figure 1 suggest that this is a reasonable assumption, except for a complex step over area north of Brawley, which we mask out in our analysis. Because of the properties of radar reflectors on the ground, well-correlated pixels from ascending and descending tracks are not always colocated. Therefore, we first resample the geocoded data with 30 m posting to a coarser 120 m posting using a median filter to maximize the number of colocated pixels in the final results. Figure 3 shows the results of the velocity decomposition for two independent pairs of ascending and descending tracks, assuming the direction of horizontal motion along the average strike of the Imperial Fault (N36.5°W).

In addition to the long-wavelength tectonic signal and visible creep along the Superstition Hills and Imperial Faults, we note significant nontectonic motion near areas of active geothermal energy production. In particular, the East Mesa and Heber geothermal areas are associated with significant subsidence visible in all four LOS velocity maps in Figure 2; this subsidence was also noted by *Taylor et al.* [2013]. As seen in Figures 3b and 3d, subsidence rates exceeding 5 mm/yr are associated with these geothermal areas, with some uplift also visible nearby, possibly related to reinjection [*Lohman and McGuire*, 2007; *Eneva et al.*, 2013; *Taylor et al.*, 2013]. The horizontal velocities (Figures 3a and 3c) are much less affected by contributions from nontectonic sources than the LOS velocities (Figure 2, although some anomalies remain. This may be due to a horizontal component of motion related to subsidence or possibly a temporal aliasing effect due to the different observation times of the ascending and descending tracks.

2.2. GPS and Trilateration Data

The M_w 6.6 1979 Imperial Valley earthquake was intensively studied by the U.S. Geological Survey, California Division of Mines and Geology and others, with results reported in USGS Professional Paper 1254 (1982). The results include both detailed field observations of coseismic surface slip [*Sharp et al.*, 1982] and geodetic measurements of afterslip at several locations along the fault.

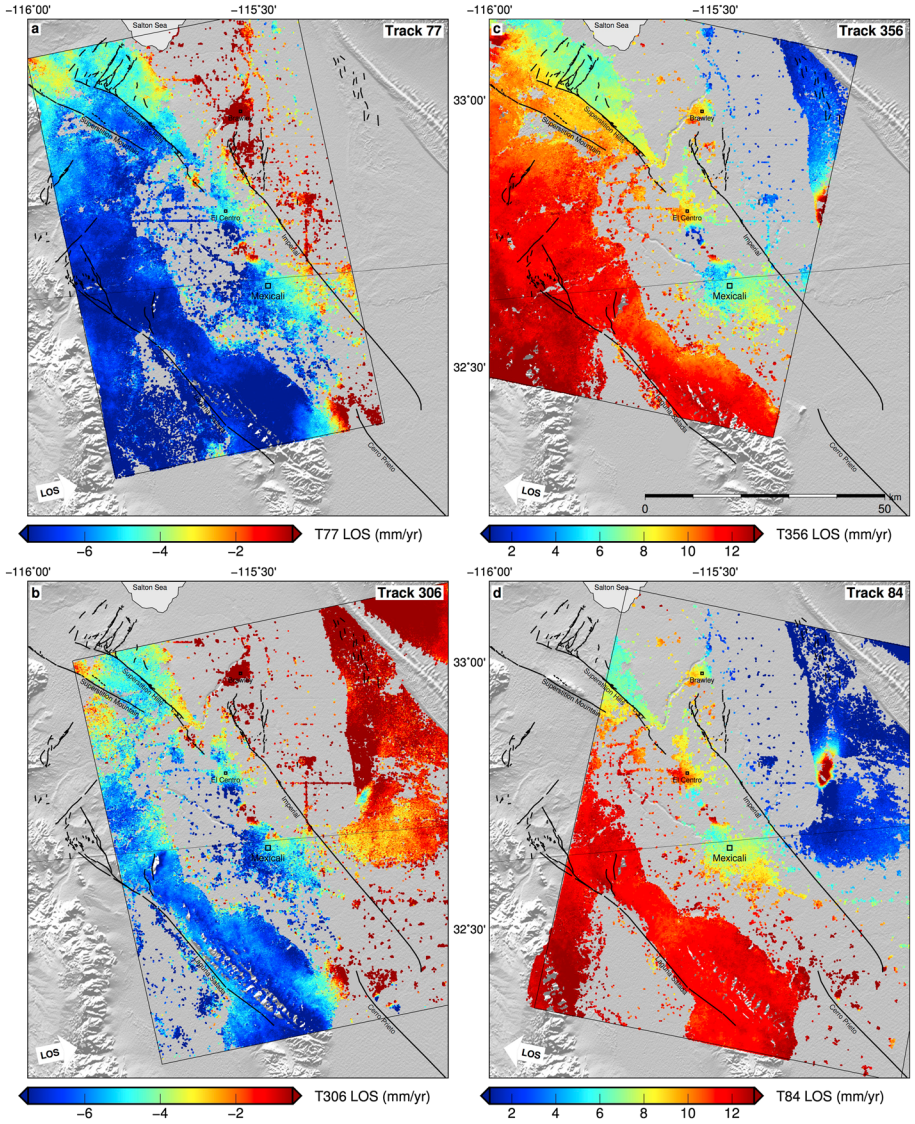

Figure 2. Estimated LOS velocities over the period 2003–2010 for Envisat tracks: (a) 77, (b) 306, (c) 356, and (d) 84 covering the Imperial Valley, computed using a persistent scatterers method [*Hooper et al.*, 2004]. Scenes collected after the 4 April 2010 M_w 7.2 Sierra-El Mayor earthquake were excluded from the analysis.

Crook et al. [1982] conducted several surveys of a trilateration array across the Imperial Valley that had been installed prior to the earthquake and recorded both the coseismic and postseismic displacements close to the fault, although their first resurvey did not take place until 1 week following the earthquake. *Harsh* [1982] installed alignment arrays across the fault at several locations within 3 days following the earthquake and recorded afterslip accumulated during the following 2 months. Together, the observations record robust shallow afterslip amounting to more than 15 cm over the first 2 months, in excess of the afterslip observed at Parkfield following the 1966 and 2004 earthquakes there [*Scholz et al.*, 1969; *Langbein et al.*, 2006].

In addition, we use interseismic velocities from a dense network of GPS monuments in the Imperial Valley, maintained by the Scripps Orbit and Permanent Array Center (SOPAC) and the UNAVCO Plate Boundary Observatory (PBO). Observations are reported in a stable North American reference frame and are available online (http://pbo.unavco.org/data/gps). We also combine survey-mode GPS velocities from the Southern California Earthquake Center Crustal Motion Map 4 [*Shen et al.*, 2011] with a set of campaign data collected and analyzed by *Lyons et al.* [2002] and *Crowell et al.* [2013]. The locations of continuous sites are shown in red and campaign sites in blue in Figure 1.

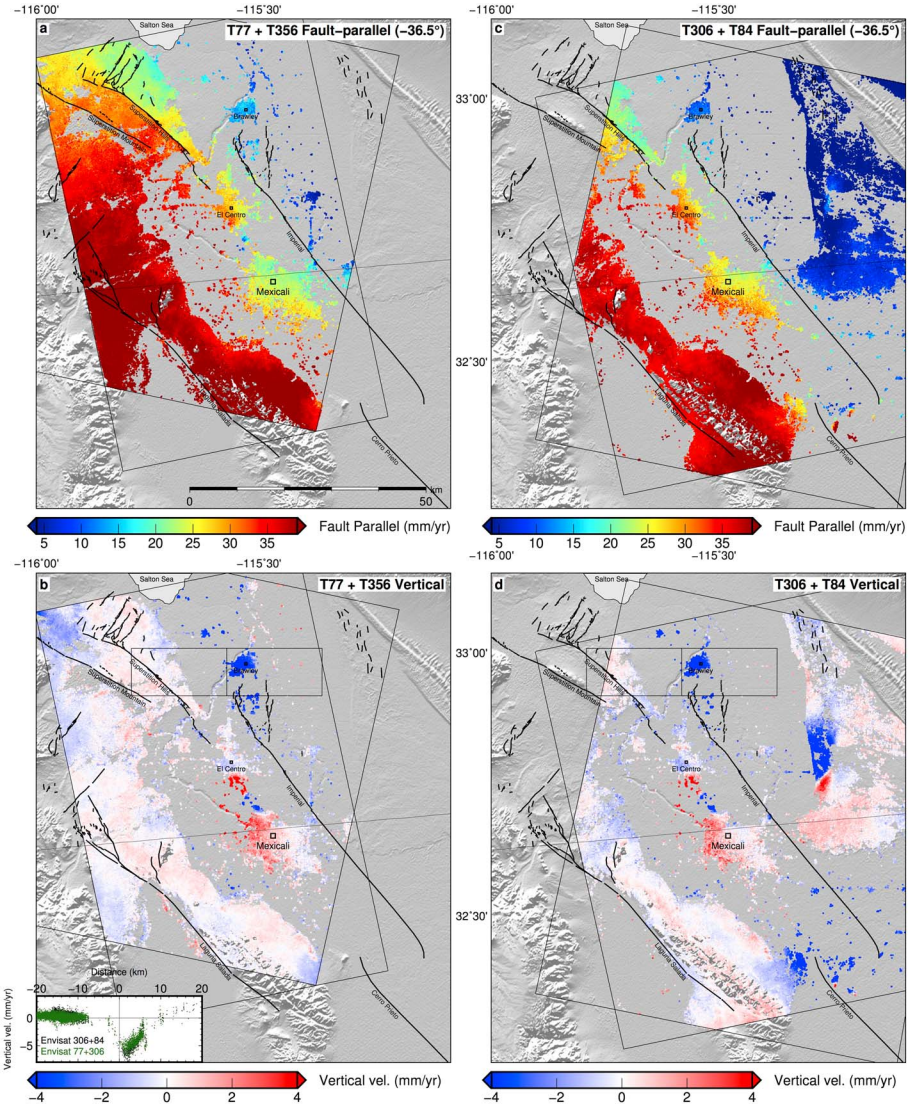

Figure 3. Vertical and fault-parallel components of Envisat InSAR observations derived from a combination of two opposing LOS directions (Figure 2) using the method of *Lindsey et al.* [2014], assuming a constant horizontal direction of motion of N36.5°W. (a) and (b) show the result derived using tracks 77 and 356, while (c) and (d) show the result using tracks 306 and 84.

2.3. Interseismic Creep Rate

Interseismic creep on the Imperial Fault has been well documented since it was first observed there in the 1950s [*Whitten*, 1956]. Unlike triangulation and GPS data which can be used to measure horizontal displacements directly, observations of creep using InSAR are complicated by the possibility of differential vertical motion across the fault (Figure 3). By combining the estimated fault-parallel InSAR velocities derived above with campaign GPS velocities where available, we obtain an accurate estimate of the strike-slip creep rate along the northernmost 40 km of the fault.

We select data within a series of 4 km wide, 12 km long profiles across the fault. The profiles are partially overlapping and spaced every 1 km along the length of the fault for which there are InSAR observations from all four tracks, resulting in a total of 43 profiles. The profiles are long enough to be affected by strain accumulation due to long-term fault motion, which adds a trend to the data on either side of the fault. The velocity and strain rate profiles are not necessarily symmetric with respect to the fault trace, as discussed below. To avoid biasing the creep rate estimation, we therefore adopt the method used by *Kaneko et al.* [2013]: we fit a linear trend to the data on either side of the fault and compute the offset between the fitted lines at the

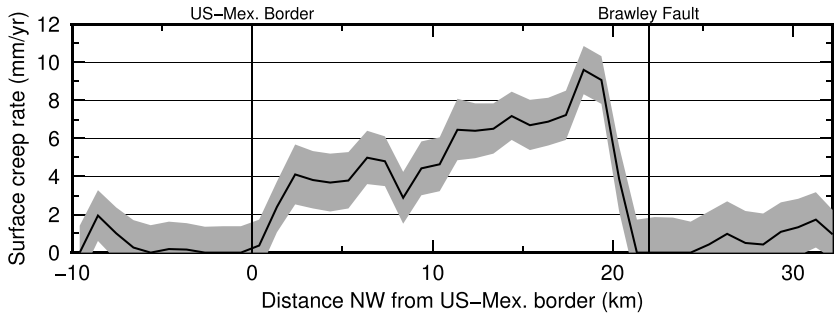

Figure 4. Creep rate along the Imperial Fault estimated from fault-parallel InSAR and GPS velocities. Gray shaded area indicates the estimated measurement uncertainty.

location of the fault trace. For each profile, we compute the creep rate for each of the two fault-parallel data sets described above (Figure 3) and combine the results in a least squares sense.

The results are shown in Figure 4. Uncertainties are computed as the standard deviation of the residuals for each profile and are shown as the gray area surrounding the best fit creep rate. Surface creep appears to take place only north of the U.S.-Mexico border, consistent with paleoseismic observations that show no evidence of slip except for the 1940 event just south of the border [*Thomas and Rockwell*, 1996]. The rate is typically between 3 and 8 mm/yr and reaches a maximum of 9-10 mm/yr toward the north, in good agreement with earlier observations [*Whitten*, 1956; *Lyons et al.*, 2002; *Crowell et al.*, 2013].

Farther to the north, creep appears to stop just before the intersection of the Brawley Fault. However, the InSAR data in this area have a lower than average number of persistent scatterers. Also, in 1979 coseismic slip along this part of the fault had a significant dip-slip component, producing subsidence of the Mesquite basin located between the Imperial and Brawley Faults [*Sharp and Lienkaemper*, 1982]. Therefore, the northern terminus of creep is not well established.

2.4. Strain Asymmetry

Two fault-perpendicular profiles across the InSAR and GPS velocity field are shown in Figure 5. The profiles are 30 km wide and include data crossing the fault to the north and south of the international border, respectively. The far-field geodetic data indicate that the relative motion across the Imperial Valley is at least 35–40 mm/yr. As the Imperial Fault is the only mapped active structure at this latitude, this value is typically accepted as a lower bound on its slip rate, and estimated rates of 40 mm/yr or higher are not uncommon [e.g., *Bennett et al.*, 1996; *Smith and Sandwell*, 2003; *Becker et al.*, 2005; *Meade and Hager*, 2005; *Smith-Konter et al.*, 2011].

We fit a simple elastic dislocation model [*Savage and Burford*, 1973] to the data using the method of *Lindsey et al.* [2013]. We assume a homogeneous elastic half space with dislocations slipping at a constant rate s below the locking depth d_L, at a location x_L that is assumed known. Creep is also permitted at a rate c between the surface and an assumed depth d_C, with the creeping fault trace at horizontal location x_C. The resulting model includes three free parameters (s, c, d_L), plus a vertical offset value v_0 corresponding to a choice of reference frame:

$$v(x) = v_0 + \frac{s}{\pi}\tan^{-1}\left(\frac{x - x_L}{d_L}\right) + \frac{c}{\pi}\left[\text{sign}(x - x_C) - \tan^{-1}\left(\frac{x - x_C}{d_C}\right)\right] \quad (1)$$

The function sign(x) returns $+1$ or -1 where x is positive or negative, respectively. The best fitting model is found using a Bayesian Monte Carlo method described by *Neal* [2003]; for its implementation see *Lindsey et al.* [2013]. Before inverting, the InSAR data are first resampled at a constant 0.5 km across-fault spacing by replacing the data with the mean and standard deviation of all pixels within each distance bin. The standard deviation within each bin is used as the uncertainty for that point in the inversion. We combine the GPS and InSAR data by weighting each measurement by its own uncertainty and do not impose an additional data-set-specific weight; however, we seek to ensure that some GPS velocities with extremely small uncertainties do not bias the model by imposing a minimum uncertainty of 1 mm/yr in the inversion. Finally, we also include the effect of the Elsinore/Laguna Salada fault, located 35 km west of the Imperial Fault, by adding a fixed 3 mm/yr dislocation with a 10 km locking depth at that position. This is the same method as adopted by *Lindsey et al.* [2013] to incorporate the contribution from this less active fault and is based on geodetic and geologic estimates of the slip rate for this fault [*Petersen and Wesnousky*, 1994; *Lindsey and Fialko*, 2013].

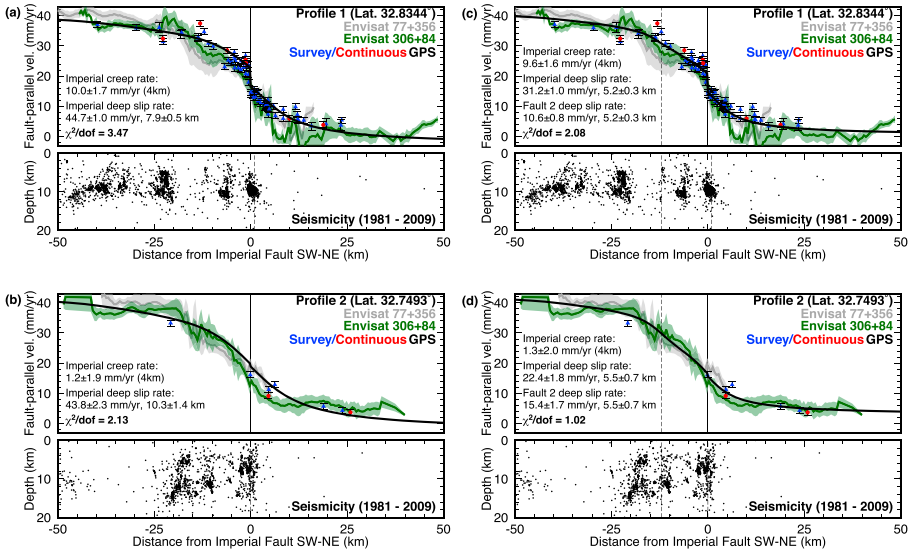

Figure 5. Two profiles across the Imperial Fault showing InSAR-derived fault-parallel velocities from tracks 77+306 (gray) and tracks 306+84 (green), and GPS velocities from survey monuments (blue) and continuous stations (red). Figures include (a, b) a best fitting dislocation model with one fault (location shown as dashed line) and (c, d) a best fitting model with two faults (dashed lines). Model uncertainties are 2σ confidence intervals. Microseismicity are from *Hauksson et al.* [2012].

The results are shown in Figure 5, considering the case of a single Imperial Fault strand in Figures 5a and 5b. The fault trace is located at $x_C = 0$, and the assumed depth of creep is $d_C = 4$ km. For the northern profile, seismicity indicates that the fault is dipping slightly to the East, so we allow the deep dislocation to be offset by $x_L = 1$ km. The best fitting creep rate is 10 ± 1.7 mm/yr (2σ uncertainty), slightly higher than the measured values in Figure 4. The deep slip rate is nearly 45 mm/yr, close to the full rate of relative motion between the Pacific and North American plates [e.g., *DeMets et al.*, 1994]. For the southern profile, the inferred creep rate is indistinguishable from zero, as expected; the deep slip rate is slightly lower than that for the northern profile, possibly due to the relatively shorter width of both the InSAR and GPS profiles in this area.

In both cases, there is a systematic misfit between the model and the data. The total geodetic strain accumulated to the west of the fault is significantly higher than that to the east in both profiles; in the southern case as much as 80% of the strain is accumulated to the west of the fault, while the model must place 50% on either side. This strain asymmetry does not coincide with any seismically observed contrast in material properties across the fault [*Fuis et al.*, 1984], nor does it coincide with significant topography that could result in differential tropospheric delays in the InSAR. One possible explanation is an active subparallel fault to the west of the Imperial Fault. As noted by *Magistrale* [2002], there are several active lineaments of seismicity to the west of the Imperial Fault which extend southward from the mapped traces of the Superstition Hills and Superstition Mountain branches of the San Jacinto Fault. Seismicity from the *Hauksson et al.* [2012] catalog (excluding aftershocks of the 2010 M_w 7.2 El Mayor-Cucapah earthquake) are shown as subpanels in Figure 5. The asymmetry in seismicity is clearly evident in both profiles.

Motivated by this observation, we consider a dislocation model with two active faults as shown in Figures 5c and 5d. We assume that the locking depths are the same for both faults. We initially considered the location of the second fault as a free parameter. The best fitting location was similar in the two profiles (11.7 ± 0.6 km and 12.4 ± 1.8 km west of the Imperial Fault for profiles 1 and 2, respectively), but the addition of this parameter introduced strong trade-offs with the fault slip rates. We therefore fix the location of the second fault at a distance of 12 km from the Imperial Fault, corresponding to a location with both a higher rate of microseismicity and geodetic strain rate in both profiles. The slip rate of the second fault s_2 is considered as an additional free parameter:

$$v(x) = v_0 + \frac{s_1}{\pi}\tan^{-1}\left(\frac{x - x_{L1}}{d_L}\right) + \frac{s_2}{\pi}\tan^{-1}\left(\frac{x - x_{L2}}{d_L}\right) + \frac{c}{\pi}\left[\text{sign}(x - x_C) - \tan^{-1}\left(\frac{x - x_C}{d_C}\right)\right] \quad (2)$$

Because this model has an additional free parameter, a better fit to the data is expected, regardless of whether the model is more representative of the underlying tectonic processes. We can assess whether the improvement in misfit is significant using the Akaike Information Criterion (AIC) [*Akaike*, 1974], defined as $2k - 2\ln(L)$, where k is the number of model parameters and $\ln(L)$ is the log likelihood (defined as $\exp(-\chi^2/N)$) of the best fitting model. In this case, we find that the improvement in fit is significant for both profiles (the AIC value improves from 14.94 to 14.16 for profile 1, and from 12.26 to 12.04 for profile 2), suggesting that the addition of a second fault to the model does capture the underlying fault behavior in this region, although the improvement is not large enough to formally rule out the first model.

The inclusion of the additional fault reduces the deep slip rate of the Imperial Fault significantly, while the creep rate is relatively unchanged. The inferred slip rate of the proposed fault varies between the two profiles, increasing toward the south from 10.6 ± 0.8 mm/yr to 15.4 ± 1.7 mm/yr. Given the simplicity of this model these rates are not intended to be definitive, but we note that they are in reasonable agreement with inferred slip rates of 10–18 mm/yr for the San Jacinto fault farther north [*Blisniuk et al.*, 2010; *Janecke et al.*, 2010; *Lindsey and Fialko*, 2013; *Lindsey et al.*, 2013]. In our proposed model, this fault transfers slip directly between the San Jacinto fault and the Cerro Prieto fault to the south, eliminating the need for a large transpressional step at the northern end of the Imperial Fault.

3. Earthquake Cycle Models

Kinematic inversions for fault slip rates using geodetic data, such as the model proposed above, have the advantage of a small number of free parameters and are generally successful at explaining the geodetic data in a statistical sense [e.g., *Meade and Hager*, 2005; *Fay and Humphreys*, 2005; *Lindsey et al.*, 2013; *Smith-Konter et al.*, 2011]. However, these models involve strong assumptions about the slip distribution with depth that limit their use in understanding the fault properties that drive such slip. An alternative method is to use numerical models incorporating rate- and state-dependent friction to simulate earthquake cycles on the fault. In these models, the fault stress and rate of slip at all times during an earthquake cycle are estimated in a self-consistent manner, avoiding the dependence on an assumed slip distribution with depth or on an assumed unphysical prestress.

Such models can provide more physical insight into the processes of interseismic slip, shallow fault creep, and afterslip but are computationally intensive and contain many more free parameters. The solution may therefore be highly nonunique; this is particularly true if data from only part of the earthquake cycle are used. For example, *Kaneko et al.* [2013] used fully dynamic earthquake cycle models to infer frictional parameters on the Ismetpasa segment of the North Anatolian fault and found that a wide range of parameters could provide an adequate fit to the interseismic data. The set of models consistent with interseismic data may produce very different predictions about the coseismic and postseismic slip, however. For this reason, well-constrained models require precise geodetic observation from all phases of the earthquake cycle. The Imperial Fault is one of a few examples for which the respective data are available.

3.1. Model Setup

We consider a vertical fault in a homogeneous elastic half space, governed by rate- and state-dependent friction, with shear stress $\tau(z,t)$ given by

$$\tau(z,t) = \sigma(z)\left[f_0 + a(z)\ln\frac{V(z,t)}{V_0} + b(z)\ln\frac{V_0\theta(z,t)}{D_c}\right] \tag{3}$$

The evolution of the state variable θ is governed by the aging law [*Dieterich*, 1992; *Ampuero and Rubin*, 2008]:

$$\frac{\mathrm{d}\theta(z,t)}{\mathrm{d}t} = 1 - \frac{V(z,t)\theta(z,t)}{D_c} \tag{4}$$

The effective shear stress $\tau(z,t)$ on the fault is given by equation (1) of *Lapusta et al.* [2000] and includes the radiation damping approximation, which subtracts a term proportional to the slip velocity $V(z,t)$ so that the integral over the past history of fault slip can be evaluated without encountering singularities. We solve these equations using the fully dynamic adaptive time stepping method described by *Lapusta et al.* [2000], with a distribution of parameters as shown in Figure 6. The model domain extends to a depth of 24 km, below which the plate is driven at the constant rate V_{pl}. The grid size is 12 m, much smaller than the minimum nucleation

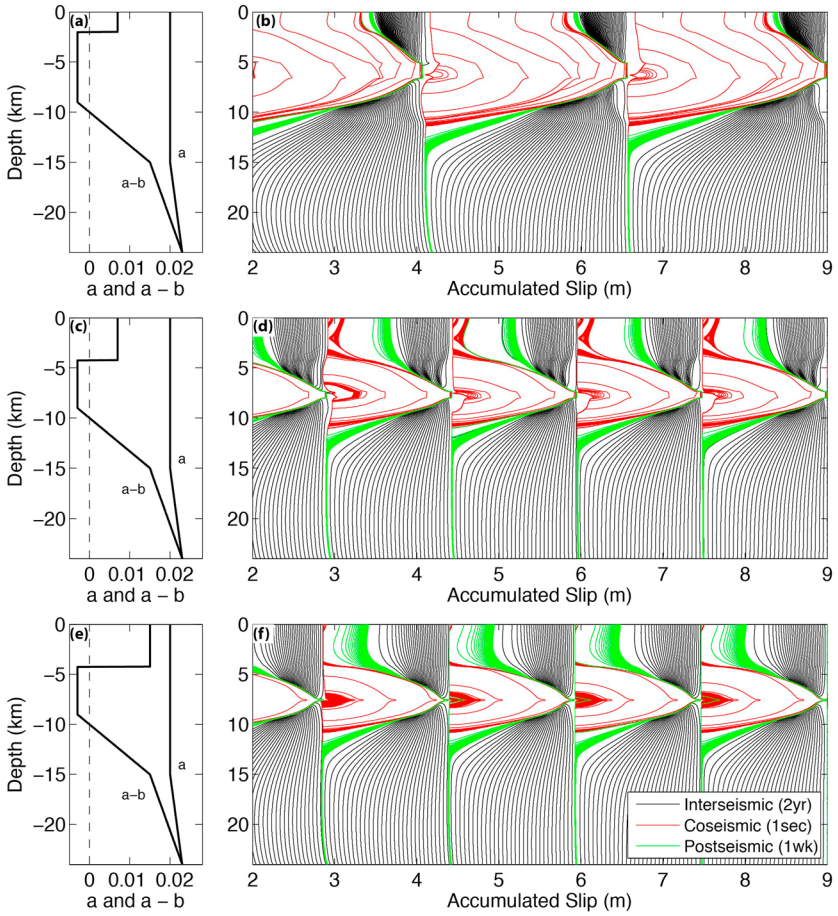

Figure 6. Modeled fault properties and accumulated slip on the fault for three scenarios with a deep fault driving rate of 25 mm/yr. (a, b) Velocity-strengthening layer with $(a - b) = 0.007$ extending to a depth of 2 km. Recurrence interval is 96 years. (c, d) Velocity-strengthening layer with $(a - b) = 0.007$ extending to a depth of 4.25 km. Recurrence interval is 61 years. (e, f) Velocity-strengthening layer with $(a - b) = 0.015$ extending to a depth of 4.25 km. Recurrence interval is 61 years. Scenario parameters are labeled 1, 2, and 3, respectively in Figure 8.

size [see *Lapusta et al.*, 2000], ensuring a numerically stable solution. In some cases, where stability permitted, we used a grid size of 24 m for computational efficiency. We also ran several test cases with a grid size of 3 and 6 m and verified that the results were independent of the model discretization.

The initial distribution of shear stress is given by equation (3) for the case of steady sliding,

$$\tau(z, t_0) = \sigma(z)\left[f_0 + (a(z) - b(z))\log\left(\frac{V_{\mathrm{pl}}}{V_0}\right)\right] \tag{5}$$

Models are run for several earthquake cycles until the simulation reaches a cycle-invariant state; examples are shown in Figure 6. For comparison with the observations, we extract a time series of surface displacements for the final cycle. We consider two fault loading rates (V_{pl}), 35 mm/yr and 25 mm/yr. The higher rate represents the commonly accepted geodetic slip rate for the Imperial Fault, while the lower value corresponds to the case proposed above where some of the strain is accommodated on other active faults to the west. Because the dynamic model formulation is antiplane strain, we cannot directly include a second fault. The latter is expected to result in a stressing rate smoothly varying with depth across the modeled Imperial Fault and is not likely to affect the details of postseismic and interseismic slips, although it could affect the recurrence interval.

3.2. Model Results

Figure 6 shows several simulations, in which periodic earthquakes are followed by postseismic afterslip and interseismic creep. Coseismic slip is represented as red contours of displacement plotted every 1 s. Rapid postseismic afterslip occurs above and below the area of coseismic slip and is shown in green contours, plotted every 7 days. Longer-term interseismic creep is shown as black contours plotted every 2 years.

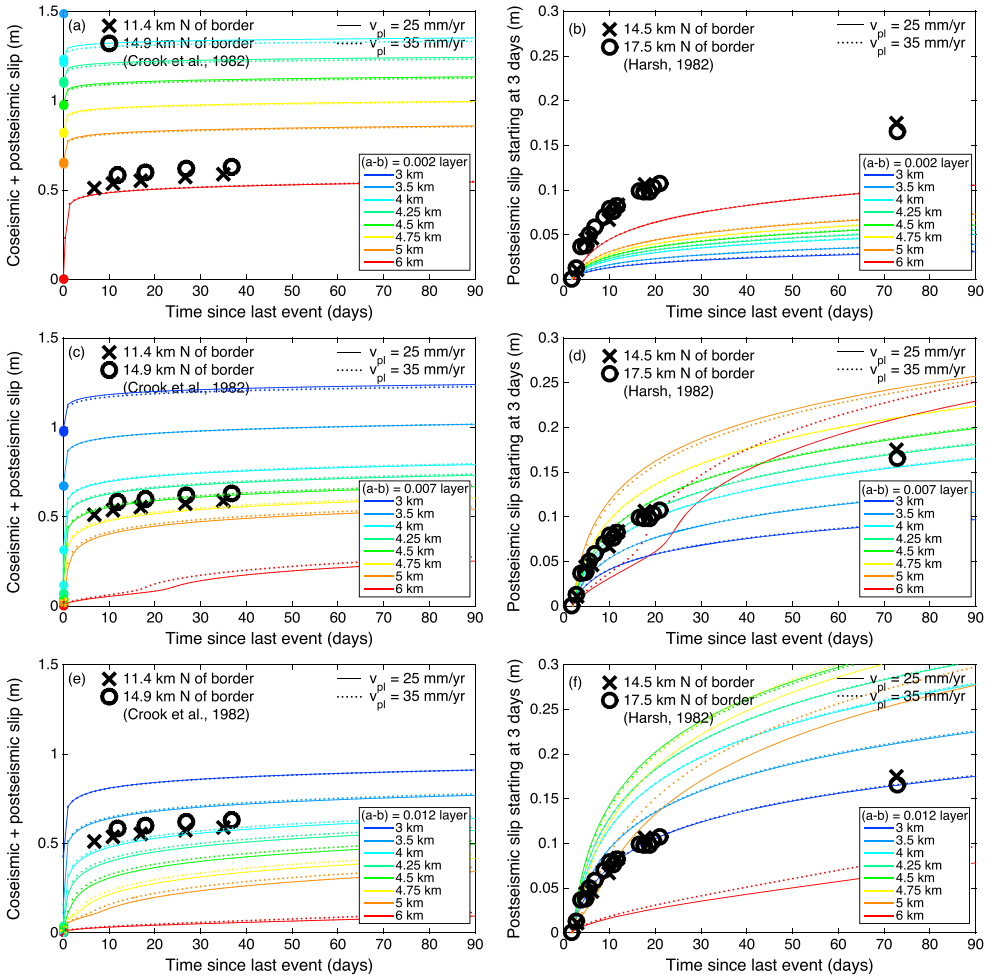

Figure 7. Model predicted surface fault slip (colored lines) compared to observations following the 1979 earthquake (symbols). (left column) The total coseismic + postseismic slip for comparison with trilateration observations by *Crook et al.* [1982]; (right column) only postseismic slip for comparison with *Harsh* [1982], starting at zero, 3 days after the event. Models where the shallow velocity-strengthening layer has (a, b) $(a-b) = 0.002$, (c, d) $(a-b) = 0.007$; and (e, f) $(a-b) = 0.012$.

We explore a range of parameters that produce earthquakes with different characteristic coseismic slip, spatial extent, and patterns of postseismic and interseismic creep. We first conducted a series of simulations which showed that the value of $(a-b)$ in the velocity-weakening (seismogenic) layer and the slip-weakening distance D_c together control the absolute size and recurrence of events but have little effect on the postseismic or interseismic slip. Changes to these values may affect the model recurrence interval but will not affect our conclusions regarding the fit of the model to interseismic and postseismic observations, which are our primary concern. Therefore, we fix these values at $(a-b) = -3\times10^{-3}$ and $D_c = 4$ mm, but note that other combinations are possible. For example, by decreasing the magnitude of $(a-b)$ while increasing D_c, the nucleation size and therefore the characteristic earthquake size and recurrence time remain nearly constant. Our chosen value of D_c of 4 mm is smaller than has typically been used in similar simulations [e.g., *Lapusta et al.*, 2000; *Lapusta and Rice*, 2003; *Kaneko et al.*, 2013] but is still larger than values of the order of 10^{-5} to 10^{-4} m estimated in laboratory studies [e.g., *Dieterich*, 1978, 1979].

Figure 7 shows modeled coseismic and postseismic displacements on the fault at the surface, along with observed displacements from the 1979 Imperial Valley earthquake. When the value of $(a-b)$ in the top velocity-strengthening layer is too small, as in Figures 7a and 7b, the model produces too much coseismic slip and not enough postseismic slip to fit the data. Conversely, when $(a-b)$ in the top layer is too large, as in Figures 7e and 7f, the model does not produce enough coseismic slip and overpredicts postseismic slip. In Figures 7c and 7d, the model with the thickest velocity-strengthening layer (6 km) shows an unusual

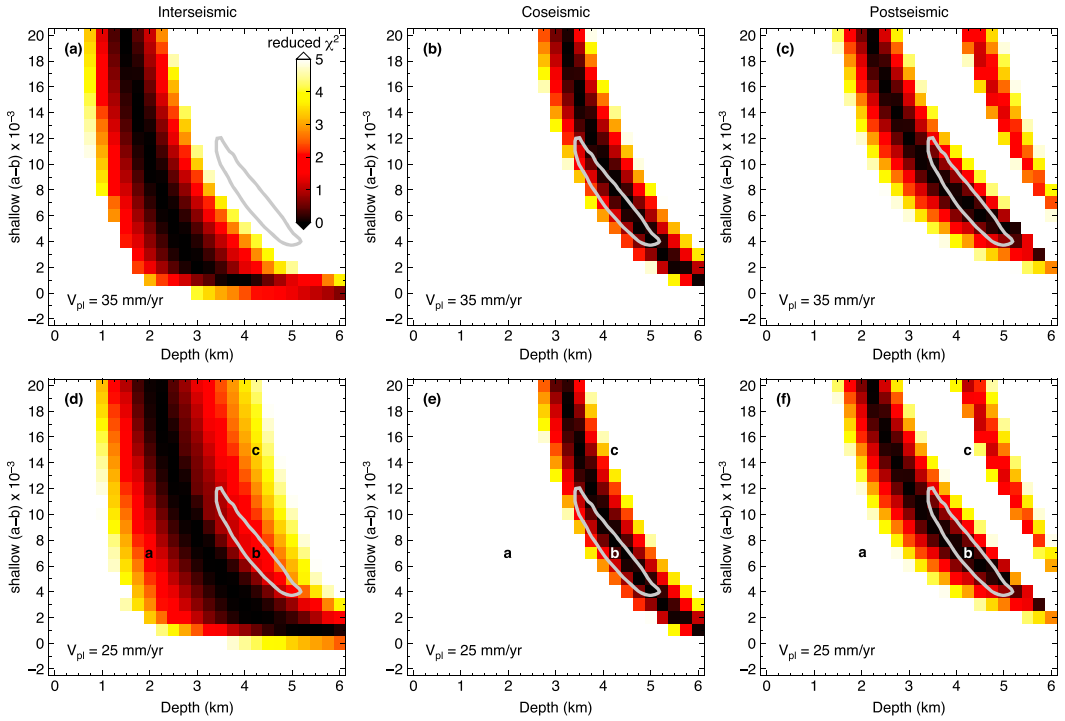

Figure 8. Panels showing the reduced χ^2 misfit (χ^2/N) to each data set for a grid search over the depth of the upper velocity-strengthening layer and values of $(a - b)$ in this layer. The fit to (a) interseismic, (b) coseismic, and (c) postseismic data for the case of a 35 mm/yr driving rate; (d–f) the case of a 25 mm/yr driving rate. Letters a, b, and c correspond to the three models shown in Figure 6. Gray contour in all panels shows the set of models with a 25 mm/yr driving rate that fit all three data sets combined; there are no such models for a 35 mm/yr driving rate (Figure 9).

acceleration of the postseismic slip after 20 days. This may be related to a stress concentration propagating slowly to the surface; a similar but much smaller delay was observed following the 2004 Parkfield earthquake, where afterslip took up to several hours to reach the surface [*Langbein et al.*, 2006].

We consider two possible values of the deep driving rate V_{pl}: 25 mm/yr and 35 mm/yr. The higher value represents the commonly accepted Imperial Fault slip rate [e.g., *Lyons et al.*, 2002; *Smith-Konter et al.*, 2011], while the lower value is motivated by the observations described in section 2.4 suggesting slip partitioning between two closely spaced faults. Figure 7 shows that the assumed deep slip rate has almost no effect on the predicted coseismic and postseismic displacements. However, the modeled interseismic creep rate is directly proportional to V_{pl}, so this parameter is a critical factor in determining the overall best fitting model.

For each model simulation, we compute a χ^2 misfit to the observations (assuming uncertainties of 10 cm/yr, 2 cm/yr, and 2 mm/yr for the coseismic, postseismic, and interseismic data sets, respectively). Modeled interseismic creep rates are taken as the minimum surface slip rate observed at any point throughout the earthquake cycle and are compared against a rate of 7 mm/yr taken from Figure 4 for the part of the fault between 10 and 15 km north of the U.S.-Mexico border, where the coseismic and postseismic observations were collected. Figure 8 shows the χ^2 misfit value to each of the three data sets for a grid search over values of $(a - b)$ in the top velocity-strengthening layer and the depth to the seismogenic layer.

The combined χ^2 misfit values for all three data sets are shown in Figure 9. We find that for the lower fault slip rate (Figure 9a), a shallow velocity-strengthening layer with values of $(a - b)$ between 4×10^{-3} and 1.2×10^{-2} and a depth between 3.5 and 5 km can fit all three observations to within the assumed uncertainty. However, for the higher fault slip rate (Figure 9b), there are no sets of parameters that can fit the observations. Comparing to Figure 8, it is apparent that the misfit is driven by a disagreement between the parameters which can fit the interseismic creep rate and those which fit the coseismic and postseismic observations. For the lower fault slip rate, the three data sets are in better agreement.

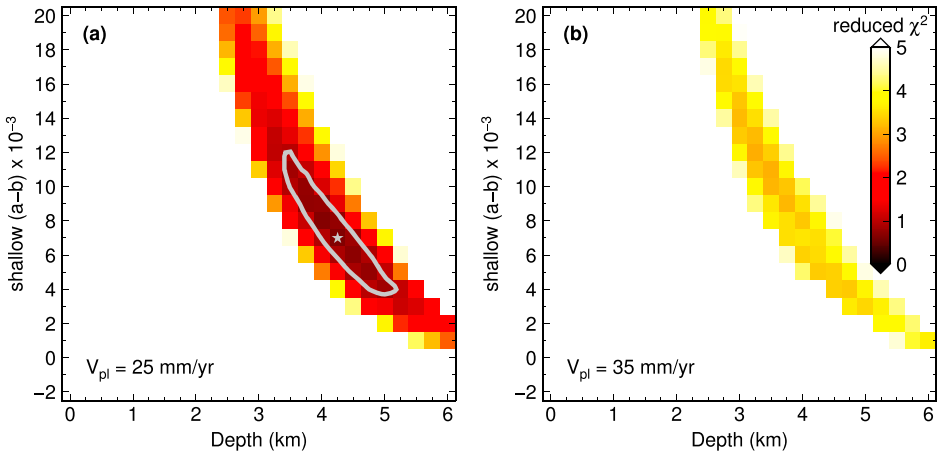

Figure 9. Reduced χ^2 misfit for the three data sets combined. The case of a (a) 25 mm/yr driving rate and (b) 35 mm/yr driving rate. Starred model corresponds to a velocity-strengthening layer depth of 4.25 km with $(a - b) = 0.007$ (shown in Figure 6b).

4. Discussion

Geodetic observations from InSAR and GPS along the Imperial Fault show that creep begins near the U.S.-Mexico border and extends northward, reaching a maximum rate of 9–10 mm/yr just south of the intersection with the Brawley Fault (Figure 4). These rates are in good agreement with previous observations of the creep at this latitude [*Whitten*, 1956; *Lyons et al.*, 2002; *Crowell et al.*, 2013]. Creep is not observed to the south of the international border. The data also show an asymmetry in the accumulation of strain with respect to the fault, suggesting that active structures to the west such as those proposed by *Hogan et al.* [2002] and *Magistrale* [2002] may accommodate a significant portion of the strain. Models incorporating a second fault to the west provide a better fit to the data (Figure 5).

A lower slip rate on the Imperial Fault implied by the two-fault model is also supported by fully dynamic simulations of earthquake cycles on a fault with rate- and state-dependent friction. As shown in Figures 8 and 9, a wide range of parameters can reproduce the observed interseismic, coseismic, or postseismic slip along the northern Imperial Fault individually, but only a much narrower range of parameters is consistent with all observations.

In our earthquake cycle models, the shallow interseismic creep rate is controlled by the depth extent and magnitude of the positive $(a - b)$ layer, and the deep driving rate V_{pl}. Although many combinations of the depth extent and magnitude of $(a - b)$ can satisfy either the coseismic, postseismic, or interseismic observations (Figures 8a and 8d), the results show that the long-term driving rate V_{pl} must be lower than the commonly inferred rate of 35 mm/yr or the models cannot fit all three sets of observations at the same time (Figure 9b). This conclusion does not depend on our choice of the slip-weakening distance D_c or the value of $(a - b)$ in the velocity-weakening seismogenic layer. These parameters affect the size and recurrence interval of ruptures on the fault but do not affect the postseismic or interseismic slip rates. This is because for quasi steady state sliding appropriate to postseismic and interseismic slips, the term containing D_c drops out of the governing equation for rate-state friction (equation (5)). This may also be seen from Figure 10, where three otherwise identical models with different D_c are compared and show virtually the same pattern of postseismic and interseismic slip despite differences in the coseismic period.

A lower Imperial Fault slip rate of 25 mm/yr is consistent with the proposal that a structure to the west accommodates ≥10 mm/yr of the relative plate motion, and thereby avoids a transpressional transfer of slip between the northern Imperial and southern San Jacinto Faults. The deformation may be localized on one or more major faults with a cryptic surface trace; although there are no mapped faults through this area, the thick sedimentary cover and agricultural disturbance may have prevented their recognition. The deformation could also be accommodated by a larger number of much smaller faults in the basement that are individually difficult to recognize at the surface. During the nearby 2010 M_w 7.2 El Mayor-Cucapah earthquake, rupture occurred on several previously unknown faults separated by just a few kilometers from the more well-known Laguna

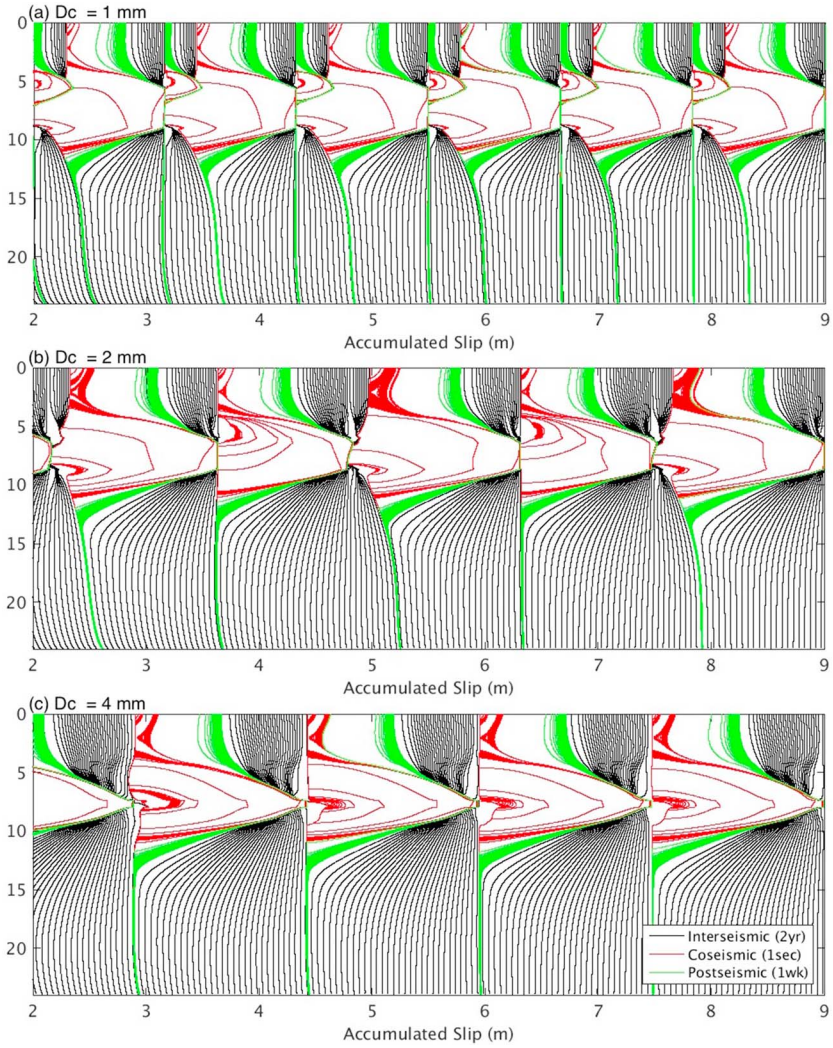

Figure 10. Models showing the effect of reducing the value of the slip-weakening distance D_c. When D_c is smaller than 4 mm as in (a) and (b), a new periodic sequence of two different-sized earthquakes develops. Models considered in the text assume $D_c = 4$ mm, as in (c). Other parameters correspond to the gray star in Figure 9.

Salada Fault [e.g., *Fletcher et al.*, 2014; *Gonzalez-Ortega et al.*, 2014], indicating that in this area multiple subparallel faults can coexist close to each other. We also note that when geodetic models of the Southern California fault system are constrained to be consistent with geologic slip rates, they commonly require as much as 30–40% of the relative plate motion to be accommodated off the major faults; this is particularly true in the Imperial Valley [see, e.g., *Bird*, 2009, Figure 6; *Johnson*, 2013].

In the case of a 25 mm/yr Imperial Fault slip rate, the best-fitting depth of the velocity-strengthening layer in our models is 4.25 $\pm$ 1 km, in good agreement with the 4–4.5 km depth extent of sediment inferred from a seismic refraction survey across this part of the Imperial Fault [*Fuis et al.*, 1984]. This is encouraging, given that a rheological change in the fault properties is likely to be correlated with a change in geological structure and composition. However, the micromechanical justification for the sediments to be velocity strengthening is not clear. Moreover, the thick sedimentary cover continues and even deepens south of the U.S.-Mexico border, where creep is not observed.

One explanation for this transition is suggested by the observation that the extent of shallow creep coincides approximately with the shoreline of ancient lake Cahuilla during its last highstand [*Luttrell et al.*, 2007]. There may thus be a gradient in the type of sediments along strike, with higher-energy deposition of fluvial sediments from the Colorado River dominating toward the south and lacustrine sediment from lake Cahuilla toward the north. It is possible that the presence of layered, silty sediment and intermittent flooding of the

lake have resulted in higher pore fluid pressure along the northern portion of the fault; elevated pressure has been proposed as a mechanism for enabling aseismic creep and slow slip events elsewhere [e.g., *Liu and Rice*, 2007; *Gomberg et al.*, 2010; *Peacock et al.*, 2011; *Frank et al.*, 2015].

The natural variability of earthquake size and recurrence rate is not reproduced by our simplified model of the fault, which generates periodic model-spanning events for the range of parameters considered above (Figure 6). Numerical experiments with a smaller value of D_c (and hence a smaller nucleation size) show that the model can produce a more complex sequence of alternating large and small earthquakes (Figure 10) (also see *Lapusta and Rice* [2003]). Nevertheless, we believe that the periodic earthquake sequences considered above are an appropriate simplification for the northern Imperial Fault, because the seismogenic zone is geometrically simple and confined to a relatively narrow depth interval, similar to the Parkfield segment of the San Andreas Fault [*Johansen et al.*, 2006; *Barbot et al.*, 2012]. The result is that the loading conditions on the seismic asperity are more isolated from time-dependent stresses elsewhere, leading to the occurrence of quasi-regular earthquakes [e.g., *Chen and Lapusta*, 2009].

Paleoseismic evidence suggests that the northern Imperial Fault does host events similar to or slightly larger than the 1979 M_w 6.6 earthquake relatively frequently (80–100 years), although the interval is somewhat variable [*Rockwell et al.*, 2011; *Tsang et al.*, 2011]. The recurrence rate is in relatively good agreement with our model results, though the variability likely reflects additional complexities that we have not accounted for. At the latitude of the U.S.-Mexico border, evidence suggests a smaller number of large, infrequent earthquakes similar to the 1940 M_w 7.0 event with a longer recurrence interval of several hundred years [*Thomas and Rockwell*, 1996]. Despite its much larger size, the 1940 earthquake produced approximately the same coseismic slip on the northern section as the 1979 earthquake [*Rockwell and Klinger*, 2013], suggesting that the behavior of these two segments is isolated from one another even when they rupture together.

Some additional complexity may result from strong dynamic weakening [*Rice*, 2006; *Beeler et al.*, 2008; *Brown and Fialko*, 2012], which can affect seismic stress drops and recurrence intervals. Numerical simulations incorporating this effect tend to produce larger, less frequent earthquakes and more coseismic slip in nominally stable parts of the fault [*Noda and Lapusta*, 2010, 2013]. In the presence of strong dynamic weakening, our model would require a smaller or less velocity-weakening seismogenic zone to compensate for the increased magnitude of coseismic slip. Because strong dynamic weakening involves a threshold of slip or slip rate, one may speculate that it is responsible for the difference between 1979- and 1940-type events on the southern portion of the Imperial Fault. Models incorporating this effect, along with two-dimensional variations in frictional properties [e.g., *Noda and Lapusta*, 2013] or the stressing influence from the proposed continuation of the San Jacinto-Superstition Hills fault system are left as promising subjects for future research.

5. Conclusions

We have used geodetic observations to infer in situ frictional properties on the Imperial Fault. We find that robust constraints on these properties require observations from all parts of the earthquake cycle. Our results are in good agreement with laboratory-derived values of the slip rate-dependence parameter ($a - b$), for a reasonable range of assumptions. The inferred depth extent of shallow creep is ~4 km, in close agreement with the seismically inferred depth of sediments, suggesting a compositional or pore fluid pressure control on the occurrence of stable creep.

Our results also suggest that the Imperial Fault is not the only active plate boundary structure at the latitude of the U.S.-Mexico border. Geodetic evidence suggests that significant strain is accommodated by a subparallel fault located 10–20 km west of the Imperial Fault, which slips at a long-term rate comparable to that of the San Jacinto Fault to the north. If so, this fault represents a significant unmapped hazard to the U.S. and Mexican communities of El Centro, Calexico, Heber, and Mexicali.

Acknowledgments
The authors wish to acknowledge David Sandwell and the MAINSAR mailing list for help with the InSAR data processing, and Yoshi Kaneko for providing the dynamic modeling code. This work was supported by the U.S. Geological Survey (USGS) under grant G16AP00004, the National Science Foundation (NSF) under grant EAR-1321932, and the Southern California Earthquake Center (contribution 6162). SCEC is funded by NSF cooperative agreement EAR-1033462 and USGS cooperative agreement G12AC20038. This material is based on data services provided by the UNAVCO Facility with support from the NSF and National Aeronautics and Space Administration (NASA) under NSF cooperative agreement EAR-0735156.

References

Akaike, H. (1974), A new look at the statistical model identification, *IEEE Trans. Autom. Control*, *19*(6), 716–723, doi:10.1109/TAC.1974.1100705.

Ampuero, J. P., and A. M. Rubin (2008), Earthquake nucleation on rate and state faults—Aging and slip laws, *J. Geophys. Res.*, *113*, B01302, doi:10.1029/2007JB005082.

Barbot, S., N. Lapusta, and J.-P. Avouac (2012), Under the hood of the earthquake machine: Toward predictive modeling of the seismic cycle, *Science*, *336*(6082), 707–710, doi:10.1126/science.1218796.

Baumberger, T., and C. Caroli (2006), Solid friction from stick-slip down to pinning and aging, *Adv. Phys.*, *55*(3–4), 279–348, doi:10.1080/00018730600732186.

Becker, T. W., J. L. Hardebeck, and G. Anderson (2005), Constraints on fault slip rates of the Southern California plate boundary from GPS velocity and stress inversions, *Geophys. J. Int.*, *160*, 634–650, doi:10.1111/j.1365-246X.2004.02528.x.

Beeler, N. M., T. E. Tullis, and D. L. Goldsby (2008), Constitutive relationships and physical basis of fault strength due to flash heating, *J. Geophys. Res.*, *113*, B01401, doi:10.1029/2007JB004988.

Bennett, R. A., W. Rodi, and R. E. Reilinger (1996), Global positioning system constraints on fault slip rates in Southern California and northern Baja, Mexico, *J. Geophys. Res.*, *101*, 21,943–21,960, doi:10.1029/96JB02488.

Berardino, P., G. Fornaro, R. Lanari, and E. Sansosti (2002), A new algorithm for surface deformation monitoring based on small baseline differential SAR interferograms, *IEEE Trans. Geosci. Remote Sens.*, *40*, 2375–2383, doi:10.1109/TGRS.2002.803792.

Bird, P. (2009), Long-term fault slip rates, distributed deformation rates, and forecast of seismicity in the Western United States from joint fitting of community geologic, geodetic, and stress direction data sets, *J. Geophys. Res.*, *114*, B11403, doi:10.1029/2009JB006317.

Blisniuk, K., T. Rockwell, L. A. Owen, M. Oskin, C. Lippincott, M. W. Caffee, and J. Dortch (2010), Late Quaternary slip rate gradient defined using high-resolution topography and ^{10}Be dating of offset landforms on the southern San Jacinto Fault zone, California, *J. Geophys. Res.*, *115*, B08401, doi:10.1029/2009JB006346.

Brown, K. M., and Y. Fialko (2012), 'Melt welt' mechanism of extreme weakening of gabbro at seismic slip rates, *Nature*, *488*(7413), 638–641, doi:10.1038/nature11370.

Brune, J. M., and C. R. Allen (1967), A low-stress-drop, low-magnitude earthquake with surface faulting: The Imperial, California, earthquake of March 4, 1966, *Bull. Seismol. Soc. Am.*, *57*, 501–514.

Chen, T., and N. Lapusta (2009), Scaling of small repeating earthquakes explained by interaction of seismic and aseismic slip in a rate and state fault model, *J. Geophys. Res.*, *114*, B01311, doi:10.1029/2008JB005749.

Colella, H. V., J. H. Dieterich, and K. B. Richards-Dinger (2011), Multi-event simulations of slow slip events for a Cascadia-like subduction zone, *Geophys. Res. Lett.*, *38*, L16312, doi:10.1029/2011GL048817.

Crook, C. N., R. G. Mason, and P. R. Wood (1982), Geodetic measurements of horizontal deformation on the Imperial fault, in *The Imperial Valley, California, Earthquake of October 15, 1979, U.S. Geol. Surv. Prof. Pap., 1254* edited by C. E. Johnson, C. Rojahn, and R. V. Sharp, pp. 183–192, U.S. Gov. Print. Off., Washington, D. C.

Crowell, B. W., Y. Bock, D. T. Sandwell, and Y. Fialko (2013), Geodetic investigation into the deformation of the Salton Trough, *J. Geophys. Res. Solid Earth*, *118*, 5030–5039, doi:10.1002/jgrb.50347.

DeMets, C., R. G. Gordon, D. F. Argus, and S. Stein (1994), Effect of recent revisions to the geomagnetic reversal time scale on estimates of current plate motions, *Geophys. Res. Lett.*, *21*, 2191–2194, doi:10.1029/94GL02118.

Dieterich, J. H. (1978), Time-dependent friction and the mechanics of stick-slip, *Pure Appl. Geophys.*, *116*, 790–806, doi:10.1007/BF00876539.

Dieterich, J. H. (1979), Modeling of rock friction 1. Experimental results and constitutive equations, *J. Geophys. Res.*, *84*, 2161–2168, doi:10.1029/JB084iB05p02161.

Dieterich, J. H. (1992), Earthquake nucleation on faults with rate- and state-dependent strength, *Tectonophysics*, *211*, 115–134, doi:10.1016/0040-1951(92)90055-B.

Eneva, M., D. Adams, G. Falorni, and J. Morgan (2013), Applications of radar interferometry to detect surface deformation in geothermal areas of Imperial Valley in southern California, paper presented at 38th Workshop on Geothermal Reservoir Engineering, Stanford Univ., Stanford, Calif.

Fay, N., and G. Humphreys (2005), Fault slip rates, effects of elastic heterogeneity on geodetic data, and the strength of the lower crust in the Salton Trough region, southern California, *J. Geophys. Res.*, *110*, B09401, doi:10.1029/2004JB003548.

Ferretti, A., C. Prati, and F. Rocca (2001), Permanent scatterers in SAR interferometry, *IEEE Trans. Geosci. Remote Sens.*, *39*, 8–20, doi:10.1109/36.898661.

Fletcher, J. M., et al. (2014), Assembly of a large earthquake from a complex fault system; surface rupture kinematics of the 4 April 2010 El Mayor-Cucapah (Mexico) M_w 7.2 earthquake, *Geosphere*, *10*, 797–827, doi:10.1130/GES00933.1.

Frank, W., N. Shapiro, A. Husker, V. Kostoglodov, H. Bhat, and M. Campillo (2015), Along-fault pore-pressure evolution during a slow-slip event in Guerrero, Mexico, *Earth Planet. Sci. Lett.*, *413*, 135–143, doi:10.1016/j.epsl.2014.12.051.

Fuis, G. S., W. D. Mooney, J. H. Healy, G. A. McMechan, and W. J. Lutter (1984), A seismic refraction survey of the Imperial Valley region, California, *J. Geophys. Res.*, *89*(B2), 1165–1189, doi:10.1029/JB089iB02p01165.

Gomberg, J., Cascadia 2007, and Beyond Working Group (2010), Slow-slip phenomena in Cascadia from 2007 and beyond: A review, *Geol. Soc. Am. Bull.*, *122*(7–8), 963–978, doi:10.1130/B30287.1.

Gonzalez-Ortega, A., Y. Fialko, D. Sandwell, A. Nava, J. Fletcher, J. Gonzalez-Garcia, B. Lipovsky, M. Floyd, and G. Funning (2014), El Mayor-Cucapah (M_w 7.2) earthquake: Early near-field postseismic deformation from InSAR and GPS observations, *J. Geophys. Res. Solid Earth*, *119*, 1482–1497, doi:10.1002/2013JB010193.

Harsh, P. W. (1982), Distribution of afterslip along the Imperial Fault, in *The Imperial Valley, California, Earthquake of October 15, 1979, U.S. Geol. Surv. Prof. Pap., 1254*, edited by C. E. Johnson, C. Rojahn, and R. V. Sharp, pp. 193–204, U.S. Gov. Print. Off., Washington, D. C.

Hauksson, E., W. Yang, and P. M. Shearer (2012), Waveform relocated earthquake catalog for Southern California (1981 to 2011), *Bull. Seismol. Soc. Am.*, *102*(5), 2239–2244, doi:10.1785/0120120010.

Hawthorne, J. C., and A. M. Rubin (2013), Laterally propagating slow slip events in a rate and state friction model with a velocity-weakening to velocity-strengthening transition, *J. Geophys. Res. Solid Earth*, *118*, 3785–3808, doi:10.1002/jgrb.50261.

Hogan, P., S. Lindvall, H. Magistrale, and T. Rockwell (2002), Continuity of the San Jacinto-Cerro Prieto Fault zones: Missing slip found in Mexicali?, paper presented at Annual SCEC Meeting, Southern California Earthquake Center, Los Angeles, Calif.

Hooper, A., H. Zebker, P. Segall, and B. Kampes (2004), A new method for measuring deformation on volcanoes and other natural terrains using InSAR persistent scatterers, *Geophys. Res. Lett.*, *31*, L23611, doi:10.1029/2004GL021737.

Janecke, S. U., R. J. Dorsey, D. Forand, A. N. Steely, S. M. Kirby, A. T. Lutz, B. A. Housen, B. Belgarde, V. E. Langenheim, and T. M. Rittenour (2010), High geologic slip rates since early Pleistocene initiation of the San Jacinto and San Felipe Fault zones in the San Andreas Fault system: Southern California, USA, *Geol. Soc. Am. Spec. Pap., 475*, 48 pp., Geol. Soc. of Am., Boulder, Colo.

Johansen, I. A., E. J. Fielding, F. Rolandone, and R. Bürgmann (2006), Coseismic and postseismic slip of the 2004 Parkfield earthquake from space-geodetic data, *Bull. Seismol. Soc. Am.*, *96*, 5269–5282, doi:10.1785/0120050818.

Johnson, K. M. (2013), Slip rates and off-fault deformation in Southern California inferred from GPS data and models, *J. Geophys. Res. Solid Earth*, *114*, 5643–5664, doi:10.1002/jgrb.50365.

Kampes, B. M., R. F. Hanssen, and Z. Perski (2003), Radar interferometry with public domain tools, paper presented at FRINGE 2003, vol. 3, pp. 1–10, Frascati, Italy, 1–5 Dec.

Kaneko, Y., Y. Fialko, D. T. Sandwell, X. Tong, and M. Furuya (2013), Interseismic deformation and creep along the central section of the North Anatolian fault (Turkey): InSAR observations and implications for rate-and-state friction properties, *J. Geophys. Res. Solid Earth*, *118*, 316–331, doi:10.1029/2012JB009661.

Langbein, J., J. R. Murray, and H. A. Snyder (2006), Coseismic and initial postseismic deformation from the 2004 Parkfield, California, earthquake, observed by Global Positioning System, electronic distance meter, creepmeters, and borehole strainmeters (in Special issue on the 2004 Parkfield earthquake and the Parkfield Earthquake Prediction Experiment), *Bull. Seismol. Soc. Am.*, *96*, S304–S320, doi:10.1785/0120050823.

Lapusta, N., and J. Rice (2003), Nucleation and early seismic propagation of small and large events in a crustal earthquake model, *J. Geophys. Res.*, *108*(B4), 2205, doi:10.1029/2001JB000793.

Lapusta, N., J. Rice, Y. Ben-Zion, and G. Zheng (2000), Elastodynamic analysis for slow tectonic loading with spontaneous rupture episodes on faults with rate- and state-dependent friction, *J. Geophys. Res.*, *105*(B10), 23,765–23,789, doi:10.1029/2000JB900250.

Lindsey, E. O., and Y. Fialko (2013), Geodetic slip rates in the southern San Andreas Fault system: Effects of elastic heterogeneity and fault geometry, *J. Geophys. Res. Solid Earth*, *118*, 689–697, doi:10.1029/2012JB009358.

Lindsey, E. O., V. J. Sahakian, Y. Fialko, Y. Bock, S. Barbot, and T. K. Rockwell (2013), Interseismic strain localization in the San Jacinto Fault zone, *Pure Appl. Geophys.*, *171*, 2937–2954, doi:10.1007/s00024-013-0753-z.

Lindsey, E. O., Y. Fialko, Y. Bock, D. T. Sandwell, and R. Bilham (2014), Localized and distributed creep along the southern San Andreas Fault, *J. Geophys. Res. Solid Earth*, *119*, 7909–7922, doi:10.1002/2014JB011275.

Liu, Y., and J. R. Rice (2007), Spontaneous and triggered aseismic deformation transients in a subduction fault model, *J. Geophys. Res.*, *112*, B09404, doi:10.1029/2007JB004930.

Lohman, R. B., and J. J. McGuire (2007), Earthquake swarms driven by aseismic creep in the Salton Trough, California, *J. Geophys. Res.*, *112*, B04405, doi:10.1029/2006JB004596.

Luttrell, K., D. T. Sandwell, B. Smith-Konter, B. Bills, and Y. Bock (2007), Modulation of the earthquake cycle at the southern San Andreas Fault by lake loading, *J. Geophys. Res.*, *112*, B08411, doi:10.1029/2006JB004752.

Lyons, S. N., Y. Bock, and D. T. Sandwell (2002), Creep along the Imperial Fault, Southern California, from GPS measurements, *J. Geophys. Res.*, *107*(B10), 2249, doi:10.1029/2001JB000763.

Magistrale, H. (2002), The relation of the southern San Jacinto Fault zone to the Imperial and Cerro Prieto Faults, in *Contributions to Crustal Evolution of the Southwestern United States, Geol. Soc. Am. Spec. Pap.*, vol. 365, edited by A. Barth, pp. 271–278, Geol. Soc. Am., Boulder, Colo.

Marone, C., and C. H. Scholz (1988), The depth of seismic faulting and the upper transition from stable to unstable slip regimes, *Geophys. Res. Lett.*, *15*, 621–624, doi:10.1029/GL015i006p00621.

Marone, C., C. Scholz, and R. Bilham (1991), On the mechanics of earthquake afterslip, *J. Geophys. Res.*, *96*, 8441–8452, doi:10.1029/91JB00275.

Meade, B. J., and B. H. Hager (2005), Block models of crustal motion in Southern California constrained by GPS measurements, *J. Geophys. Res.*, *110*, B03403, doi:10.1029/2004JB003209.

Neal, R. M. (2003), Slice sampling, *Ann. Stat.*, *31*, 705–767, doi:10.1214/aos/1056562461.

Noda, H., and N. Lapusta (2010), Three-dimensional earthquake sequence simulations with evolving temperature and pore pressure due to shear heating: Effect of heterogeneous hydraulic diffusivity, *J. Geophys. Res.*, *115*, B12314, doi:10.1029/2010JB007780.

Noda, H., and N. Lapusta (2013), Stable creeping fault segments can become destructive as a result of dynamic weakening, *Nature*, *493*(7433), 518–521, doi:10.1038/nature11703.

Peacock, S. M., N. I. Christensen, M. G. Bostock, and P. Audet (2011), High pore pressures and porosity at 35 km depth in the Cascadia subduction zone, *Geology*, *39*, 471–474, doi:10.1130/G31649.1.

Petersen, M. D., and S. G. Wesnousky (1994), Fault slip rates and earthquake histories for active faults in Southern California, *Bull. Seismol. Soc. Am.*, *84*, 1608–1649.

Rice, J. R. (2006), Heating and weakening of faults during earthquake slip, *J. Geophys. Res.*, *111*, B05311, doi:10.1029/2005JB004006.

Rice, J. R., and A. L. Ruina (1983), Stability of steady frictional slipping, *J. Appl. Mech.*, *50*, 343–349, doi:10.1115/1.3167042.

Rockwell, T. K., and Y. Klinger (2013), Surface rupture and slip distribution of the 1940 Imperial Valley earthquake, Imperial Fault, Southern California: Implications for rupture segmentation and dynamics, *Bull. Seismol. Soc. Am.*, *102*, 629–640, doi:10.1785/0120120192.

Rockwell, T. K., A. Meltzner, and R. Tsang, (2011), A long record of earthquakes with timing and displacements for the Imperial Fault: A test of earthquake recurrence models, *U.S. Geol. Surv. Open File Rep., G10AP00003*, Geol. Sci., San Diego State Univ., San Diego, Calif.

Ruina, A. (1983), Slip instability and state variable friction laws, *J. Geophys. Res.*, *88*, 10,359–10,370, doi:10.1029/JB088iB12p10359.

Savage, J., and R. Burford (1973), Geodetic determination of relative plate motion in central California, *J. Geophys. Res.*, *78*, 832–845, doi:10.1029/JB078i005p00832.

Schmidt, D., and R. Bürgmann (2003), Time-dependent land uplift and subsidence in the Santa Clara Valley, California, from a large interferometric synthetic aperture radar data set, *J. Geophys. Res.*, *108*(B9), 2416, doi:10.1029/2002JB002267.

Scholz, C. (2007), Fault mechanics, in *Treatise on Geophysics*, vol. 6.10, edited by G. Schubert, pp. 441–483, Elsevier, Amsterdam, doi:10.1016/B978-044452748-6.00111-5.

Scholz, C. H. (1998), Earthquakes and friction laws, *Nature*, *391*, 37–42, doi:10.1038/34097.

Scholz, C. H., M. Wyss, and S. W. Smith (1969), Seismic and aseismic slip on the San Andreas Fault, *J. Geophys. Res.*, *74*(8), 2049–2069, doi:10.1029/JB074i008p02049.

Sharp, R. V., and J. J. Lienkaemper (1982), Preearthquake and postearthquake near-field leveling across the Imperial Fault and the Brawley Fault zone, in *The Imperial Valley, California, Earthquake of October 15, 1979, U.S. Geol. Surv. Prof. Pap., 1254*, edited by C. E. Johnson, C. Rojahn, and R. V. Sharp, pp. 169–182, U.S. Gov. Print. Off., Washington, D. C.

Sharp, R. V., et al. (1982), Surface faulting in the central Imperial Valley, in *The Imperial Valley, California, Earthquake of October 15, 1979, U.S. Geol. Surv. Prof. Pap., 1254*, edited by C. E. Johnson, C. Rojahn, and R. V. Sharp, pp. 119–144, U.S. Gov. Print. Off., Washington, D. C.

Shen, Z. K., R. W. King, D. C. Agnew, M. Wang, T. A. Herring, D. Dong, and P. Fang (2011), A unified analysis of crustal motion in Southern California, 1970–2004: The SCEC crustal motion map, *J. Geophys. Res.*, *116*, B11402, doi:10.1029/2011JB008549.

Smith, B., and D. Sandwell (2003), Coulomb stress accumulation along the San Andreas Fault system, *J. Geophys. Res.*, *108*(B11), 2540, doi:10.1029/2002JB002296.

Smith-Konter, B. R., D. T. Sandwell, and P. Shearer (2011), Locking depths estimated from geodesy and seismology along the San Andreas Fault system: Implications for seismic moment release, *J. Geophys. Res.*, *116*, B06401, doi:10.1029/2010JB008117.

Taylor, H., M. E. Pritchard, and R. B. Lohman (2013), Recent changes in ground deformation at the East Mesa Geothermal Field, California as measured by InSAR, Abstracts G33D-06 presented at 2013 Fall Meeting, AGU.

Thomas, A. P., and T. K. Rockwell (1996), A 300- to 550-year history of slip on the Imperial Fault near the U.S.-Mexico border: Missing slip at the Imperial Fault bottleneck, *J. Geophys. Res.*, *101*, 5987–5997, doi:10.1029/95JB01547.

Tong, X., D. T. Sandwell, and B. Smith-Konter (2013), High-resolution interseismic velocity data along the San Andreas Fault from GPS and InSAR, *J. Geophys. Res. Solid Earth*, *118*, 369–389, doi:10.1029/2012JB009442.

Tsang, R. Y., T. K. Rockwell, A. J. Meltzner, and P. M. Figueiredo (2011), Towards development of a long rupture history of the Imperial Fault in Mesquite Basin, Imperial Valley, Southern California, *Seismol. Res. Lett.*, *82*, 273–361, doi:10.1785/gssrl.82.2.273.

Tse, S. T., and J. R. Rice (1986), Crustal earthquake instability in relation to the depth variation of frictional slip properties, *J. Geophys. Res.*, *91*, 9452–9472, doi:10.1029/JB091iB09p09452.

Wei, M., and D. T. Sandwell (2010), Decorrelation of ALOS and ERS interferometry over vegetated areas in California, *IEEE Trans. Geosci. Remote Sens.*, *48*, 2942–2952, doi:10.1109/TGRS.2010.2043442.

Wei, M., Y. Kaneko, Y. Liu, and J. J. McGuire (2013), Episodic fault creep events in California controlled by shallow frictional heterogeneity, *Nat. Geosci.*, *6*, 566–570, doi:10.1038/ngeo1835.

Wessel, P., W. H. F. Smith, R. Scharroo, J. F. Luis, and F. Wobbe (2013), Generic mapping tools: Improved version released, *Eos Trans. AGU*, *94*, 409–410, doi:10.1002/2013EO450001.

Whitten, C. A. (1956), Crustal movement in California and Nevada, *Eos Trans. AGU*, *37*(4), 393–398, doi:10.1029/TR037i004p00393.